Crack growth measurement and *J*-integral evaluation of additively manufactured polymer using digital image correlation and FE modeling

Mohamed Ali BOUAZIZ[1], Joseph MARAE DJOUDA[1-2], Marouene ZOUAOUI[1-3], Julien GARDAN[1-3], François HILD[2]

[1]ERMESS, EPF-Engineering school, 3 bis rue Lakanal, 92330 Sceaux, France

[2]Université Paris-Saclay, ENS Paris-Saclay, CNRS, LMT - Laboratoire de Mécanique et Technologie, 4 avenue des sciences, 91190 Gif-sur-Yvette, France

[3]Institut Charles Delaunay, LASMIS, UTT, UMR CNRS 6281, 12 rue Marie Curie, 10010 Troyes, France

Abstract

This paper presents and compares two combined experimental-numerical techniques for the investigation of fracture properties of additively manufactured polymer parts using digital image correlation (DIC) measurements. The first method uses only measured kinematic fields, and the second is based on Finite Element simulations driven by measured boundary conditions. A micro Single Edge Notched Tensile sample manufactured by fused filament fabrication of ABS is studied. It is shown that both methods locally extract *J*-integrals, and the crack tip is accurately located by the FE-based method. By comparing computed displacements to those measured via DIC it is possible to locally check the validity of the numerical model. The initiation and propagation stages are analyzed independently thanks to two different magnifications of acquired image series.

Keywords: Additive manufacturing; digital image correlation; finite element method; *J*-integral, crack propagation

1 Introduction

The growth of using Additive Manufacturing (AM) in the production of functional and end-use finished parts raises the level of quality requirements [1]. Therefore, the major challenge of AM research is to improve the mechanical properties using various experimental and numerical design techniques [2]. The most commonly used technology for making AM parts made of polymers is fused filament fabrication (FFF) [3,4]. The process is based on the extrusion of a thermoplastic polymer filament through a heated nozzle deposited layer-by-layer to create parts from a digital model. Acrylonitrile-Butadiene-Styrene (ABS) is the most widely used and commonly studied polymer for FFF [5].

Many studies focused on the tensile properties, although flexural [6], torsional [7], and compression [8] tests of FFF structures were reported. These studies showed that the mechanical properties depend on the material, and include geometry and processing (e.g., build orientation, raster angle, raster width, filament size, gap, and temperature) [9–16]. There are few analyses on fracture properties of AM polymer parts. Recently, there is growing interest in the understanding of fracture for 3D printed polymers. Hart et al. [17] explored the effect of layer orientation on the fracture properties of ABS obtained via FFF. The authors demonstrated that the inter-laminar fracture toughness (i.e., fracture between layers) was approximately one order of magnitude lower than the cross-laminar toughness (i.e., fracture through layers). McLouth et al. [18] analyzed how the fracture toughness varied with the mesostructure. It was concluded that the orientation of individual tracks of deposited material with respect to the crack tip had the most pronounced role in altering the fracture toughness of 3D printed ABS. Li et al. [19] confirmed that the fracture properties highly depended on the build/raster orientations. The strong influence of the printing parameters on the fracture properties implies that for any change in the parameter set requires an experimental study to be carried out to extract them. Consequently, there is an interest in defining methods to be adopted and developing tools to evaluate fracture properties in a precise and easily reproducible way.

Digital image correlation (DIC) is widely used to measure kinematic fields, due to its ease of use in a wide range of materials including AM polymeric materials. DIC has increasingly been used in fracture research. Based on the kinematic field around a crack, Cherepanov–Rice's *J*-integral [20] was used to directly calculate the energy release rate from strain fields around a crack. Catalanotti et al. [21] developed a method based on the measurement of the displacement and strain fields using DIC to measure crack resistance curves of cross-ply CFRP composite laminates. Later, Becker et al. [22] evaluated the *J*-integral from the measured crack displacement

field, which they coined JMAN. Excellent agreement with other fracture characterization techniques was achieved when testing JMAN on elastic, elastoplastic and quasi-brittle materials [22,23]. In order to evaluate the *J*-integral for a power-law hardening material, Yoneyama et al. [24] used three methods, that is, the path integral method, the domain integral method and the least squares method with the Hutchinson, Rice and Rosengren (HRR) field [20], [25]. The *J*-integral was obtained from strains and stresses computed from DIC measured displacements. Their results showed that the *J*-integral could be obtained accurately by such methods [24,26]. Some hybrid methods have also been developed [27–30]. The measured displacements were used as boundary conditions for finite element analyses. The advantages put forward by the authors of the works cited above over other methods are geometric freedom, i.e. the method can be applied to any type of tested sample [21,24,30]. It is also insensitive to inelastic strains close to the crack tip [22,23]. *J*-integral evaluations using directly the measured crack displacement field methods and/or hybrid method are likely to be transferable to AM polymeric materials.

In the present work, a combined computational and experimental investigation is performed to study the fracture behavior of 3D printed ABS specimens. A local analysis is performed to evaluate fracture mechanics parameter (i.e., *J*-integral) via displacement and strain fields using DIC and coupling them with finite element simulations. The so-called micro single edge notch tension (μ-SENT) specimen is first examined. The microscale experiment coupled with DIC is then used to measure surface displacement and strain fields [31,32]. To study the effect of the mesostructure on the fracture behavior of additively manufactured materials, numerical tools are developed here to make the best use of microscale experimental results (kinematic fields). Based on kinematic fields, crack tip location and *J*-integral are investigated by two methods. On the one hand, FE calculations are run with ABAQUS [33] using measured displacements as boundary conditions. The crack tip position is found by minimizing the error between computed and measured displacement fields. The *J*-integral is assessed with the built-in interaction integral [34,35]. On the other hand, MATLAB scripts are developed to find crack tip position and calculate the *J*-integral using the measured kinematic fields.

2 Experimental set-up and protocol

2.1 Specimen preparation

A µ-SENT specimen was 3D printed with the dimensions shown in **Figure 1(a)**. The notch was included in the 3D model in order to reproduce it by AM. The notch dimension meets ASTM E1820 [36] and ASTM D6068 [37] standard recommendations, namely, specimen width and initial crack length. The specimen was printed by adding fused filaments of Acrylonitrile Butadiene Styrene (ABS) using a Makerbot replicator 2X 3D printer. The extrusion temperature was set to 230 °C, and the fabricated plate was heated up to 110 °C. The sample was printed as a solid part, in a flat part orientation and [+/-45°] configuration (**Figure 1(b)**). The part is made up of 24 layers whose individual thickness was 0.25 mm. In order to ease the surface functionalization, the specimen was mechanically polished. The thickness of the specimen was reduced from 6 mm to 3 mm. White speckles with micrometric dimensions were deposited using an airbrush (speckle diameter varying between 10 µm and 30 µm with an average of 20 µm) [31].

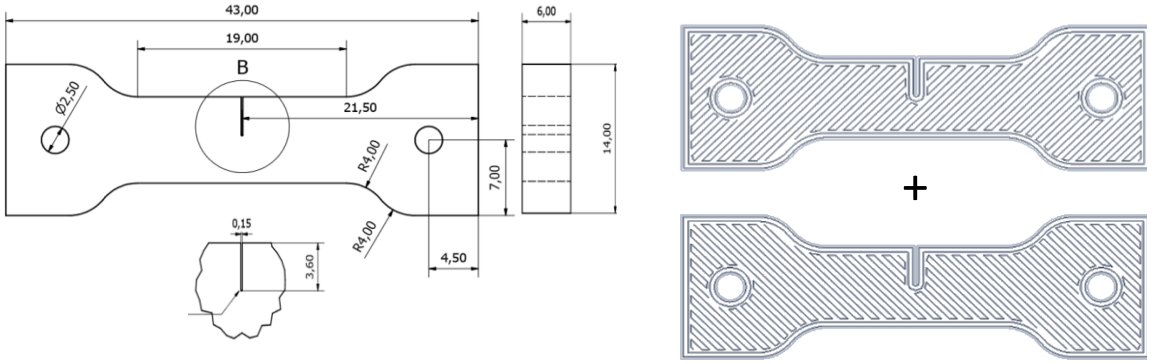

(a) µ-SENT sample dimensions (mm)

(b) +/- 45 ° deposition: +45° and -45° layers

Figure 1: *Sample geometry and raster orientations*

2.2 In situ tensile test

The experimental setup consisted of a numerical Keyence VHX-1000 microscope for surface observation, a tensile micromachine and a triggering system (**Figure 2**). The latter allowed images to be recorded at specific rates when the specimen was continuously loaded and each image to be related to the corresponding applied load. Since the notch was welded due to the temperature of filament deposition and the dimension of the notch (i.e., 150 µm in width), the magnification power was set to the lower lens range value (100×) in order to

monitor a wide enough region to contain the notch opening. When this opening was detected, a zoom (2×) in the vicinity of the notch root was operated with no interruption of the test.

During the test, one image per second was recorded until specimen failure and stored directly in tagged image file format (tiff) from the Keyence processing software. The images quality during the acquisition was satisfying and no additional treatments were required before DIC analysis. The depth in the field of the selected magnifications was sufficient because it was not necessary to change the system calibration during the test. This observation proves that the out-of-plane displacements remained very small to induce artifacts for 2D-DIC.

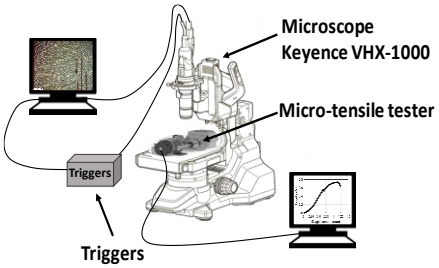

Microscope	Keyence VHX-1000	
Definition	54 Megapixel 3CCD	
Lens	VH-Z100R (100× to 1000×) Wide-range zoom lens	
Image acquisition rate	1 fps	
Pattering technique	airbrush	
Pattern feature size	20 µm	
Load cell	5 kN	
Cross-head displacement rate	1.5 µm/s	
	1st part	**2nd part**
Field of view	6.1 × 4.5 mm²	3.05 × 2.28 mm²
Image scale	4 µm/pixel	2 µm/pixel

Figure 2: *Experimental setup and hardware information*

2.3 Kinematic field measurement

DIC provides displacement fields [38]. From an image of the surface in reference and deformed states, 2D displacement vectors were retrieved by registering subsets in the original image within the deformed image. DIC resolutions are now sufficient to analyze experiments performed at various scales [39,40]. In the present study, Ncorr [41] was used to register the microscopic images obtained during the test [32].

Figure 3 shows the load vs. strain curve where ε_{yy} is the global true strain in the tensile direction. This curve is associated with some longitudinal strain maps (Euler-Almansi strain fields) in order to illustrate the main local features at the specimen surface. **Figure 3** highlights two zones. The first zone corresponds to elastic deformations of the material. This elastic response is abruptly stopped at step 562 by the load drop which is due to notch reopening. The notch of the designed specimen was not correctly printed, and the filaments of the outline,

which should make up the notch were welded when printing. Consequently, the strain was uniformly distributed on the material surface. At step 551, strain concentrations were observed around the notch, just before reaching step 562 where weld line failure occurred. The notch fully opened along its length, which was equal to 3.6 mm. At this step, a zoom was operated to focus on the root of the notch. The field of view then was changed from 6.1 × 4.5 mm² to 3.05 × 2.28 mm² (this is called part 2). In that part, the highest strain concentration was found at the root of the notch. Elsewhere, strain distributions were more uniform until step 648 where non-uniform distributions appeared. The shape of the concentration zones is probably due to the filaments deposition orientations. It appears at right angles caused by the intersection of +45° and -45° orientations. The strain is no longer concentrated only in the crack vicinity but rather in the joints between filaments. The deformation at these zones increasingly grew, thereby creating multiple cracks in welding lines that ultimately caused the global failure. The load drop caused by the global failure was progressive because of one-by-one filament failure.

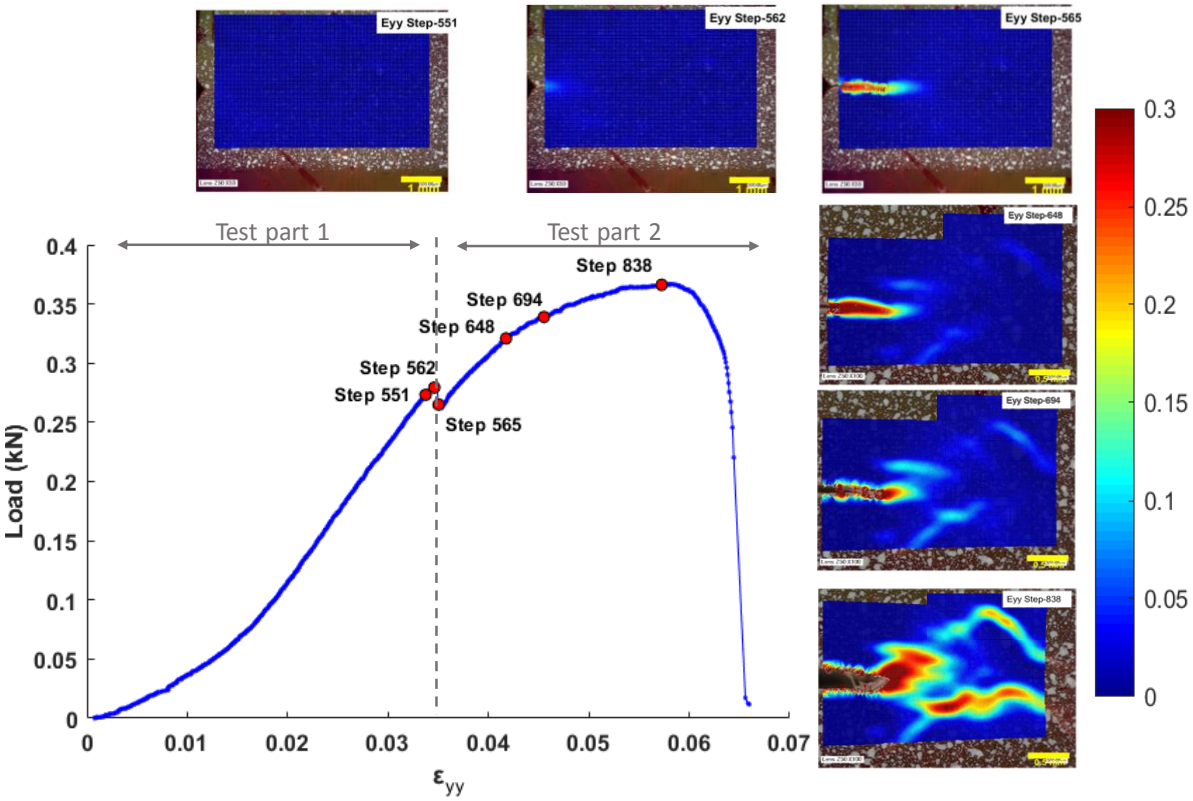

Figure 3: *Strain field analysis of fracture events and corresponding load vs. mean longitudinal strain curve*

3 Crack tip location

The first question to address when analyzing the fracture behavior is the location of the crack tip. This is an experimental challenge [43]. The most widely used technique for crack propagation monitoring is to resort to direct observations by optical means [44]. The resolution in terms of crack opening is of the order of one pixel, which can be satisfactory if an optical microscope is used. Crack growth measurement can thus be carried out with a micrometric resolution. This approach, despite its simplicity, usually is very delicate and extremely slow. On certain types of material, the visual identification of the crack tip is not obvious, which makes it imprecise. Image processing by DIC allows for crack growth measurement from subsequent analyses, or as a direct output of the correlation procedure. So-called ‘‘integrated approaches’’ (or I-DIC [45–47]) were followed to directly determine the crack tip location. Most of the approaches to measure crack growth using DIC were based on post-processing the measured displacement fields [21,29,48,49]. This approach is also used herein to locate the crack tip.

Two procedures are presented and tested on the present experiment. The first procedure is based on strain field analysis [32]. The second one uses FE calculations to determine the crack tip location by minimizing the distance between measured and computed displacement fields [29]. It belongs to the class of finite element model updating techniques [50]. The first procedure was initially presented in a previous study [32], and is applied in this study and compared to the second procedure [29], which was also utilized in the work of Vargas et al. [51].

3.1 Procedure 1 (analysis of Euler-Almansi strain maps)

In the crack vicinity, the longitudinal strain reaches its maximum level very close to the crack tip. The crack tip position can be then found by locating the maximum strain. Hereafter, it was assumed that crack growth was obtained by tracking the motion of the point of maximum in the strain maps. The center of the subset where the strain was maximum was assumed to be the crack tip if the upstream region, which is in the wake of the fracture process zone, was free of discontinuities. The main procedure steps are shown in **Figure 4**.

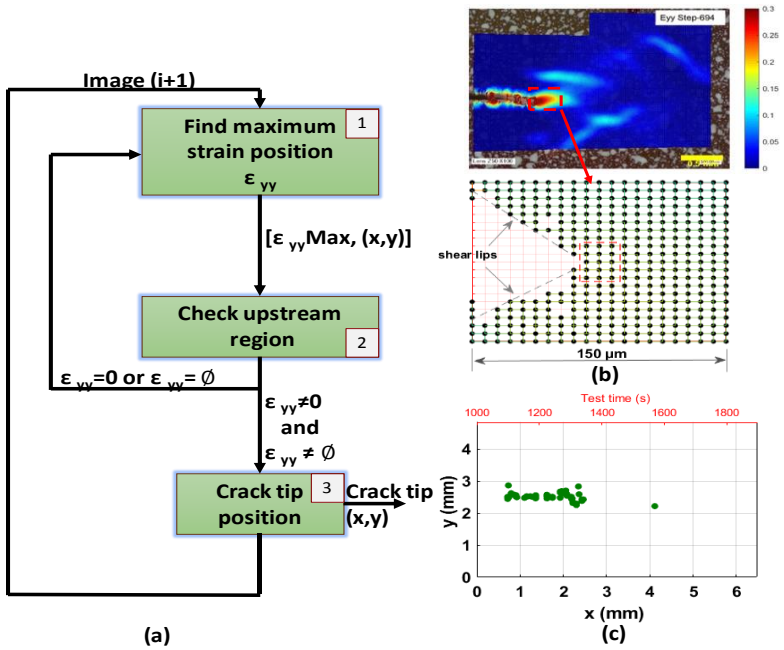

Figure 4: *(a) Crack tip location algorithm. (b) Strain matrix representation. (c) Crack tip position* [32]

3.2 Procedure 2

For this second procedure, a simple definition of the crack tip location was considered. It corresponded to the location for which the identification error between the measured ($\mathbf{u}_{meas}$) and computed ($\mathbf{u}_{comp}$) displacement fields was the smallest when the crack tip $\mathbf{x}_c$ position is changed [29]. FE calculations were conducted for every time step. Only the part inside the DIC region of interest was modeled. Boundary conditions were defined by prescribing the displacements of the external boundary of the ROI (see **Figure 5**). The computed displacements $\mathbf{u}_{comp}$ of all inner nodes are used to determine the crack tip position. The nodal displacement difference between DIC and FE analyses is computed, and the displacement gap consists in the root-mean-square difference

$$\delta^2(\mathbf{x}_c) = \frac{1}{n_m}\sum_{m=1}^{n_m}\left\|\mathbf{u}_{meas}(\mathbf{x}_m) - \mathbf{u}_{comp}(\mathbf{x}_m, \mathbf{x}_c)\right\|^2 \qquad (1)$$

where $\mathbf{x}_c$ is the considered crack tip node, n_m the number of measurements located at $\mathbf{x}_m$.

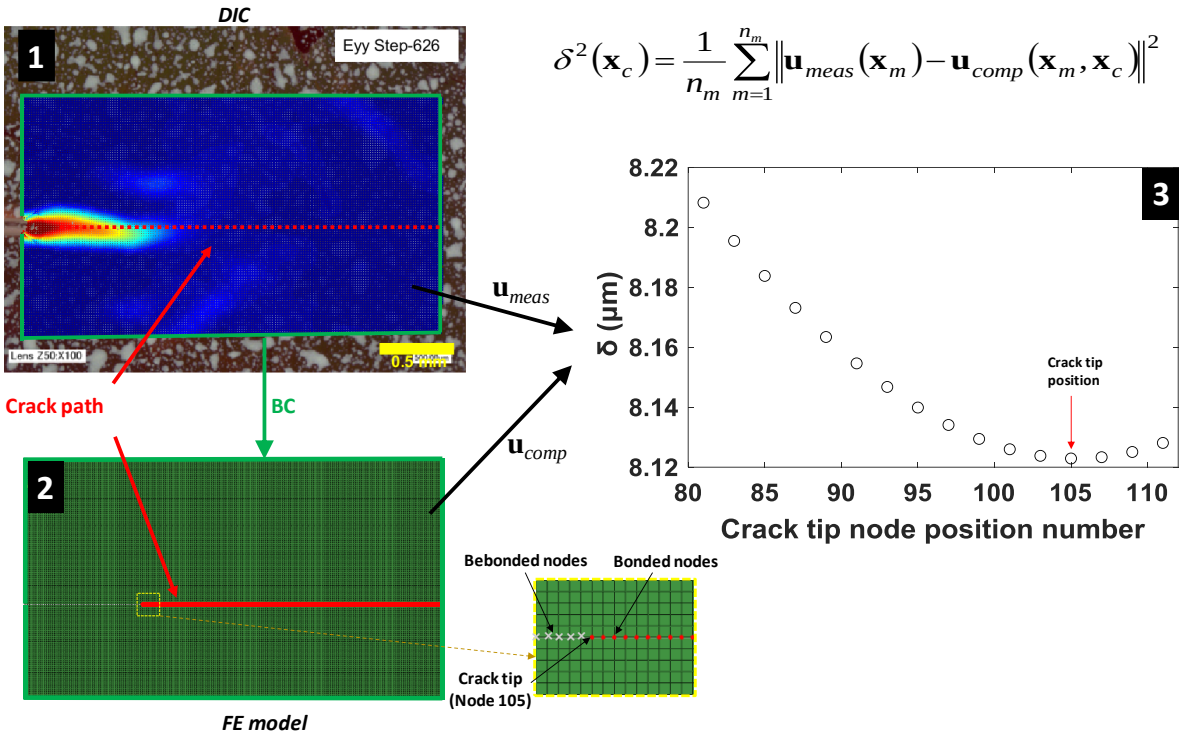

Figure 5: *Measured boundary conditions prescribed to the FE model and schematic view of the crack tip location procedure*

In the finite element model, the ROI was modeled as a 2D rectangular area meshed with four-node plane stress elements (CPS4). The mesh size is the distance between consecutive subset centers. In this way, the number of nodes in this model was identical to the number of DIC subsets (**Figure 5**). The behavior of the ABS material obtained by FDM was assumed to be elastic and orthotropic. The elastic properties of each layer are as follows, E_1 = 1680 MPa, G_{12} = 545 MPa, E_2 = 1415 MPa, ν_{12}= 0.37, where the longitudinal direction of the layer is 1, the transverse direction is 2. These values were determined by performing a series of tensile tests on [0°], [±45°], [90°] configurations. The same 3D printer and ABS filament were used to manufacture those samples. The printing parameter set was also preserved [32,52].

For each load step, several crack tip positions were considered along the crack path. For each chosen position, an FE calculation was performed to obtain the nodal displacements. Then, these displacements were compared to those measured by calculating the identification error (1). The FE result that was closest to reality yields the smallest error. **Figure 6** shows the identification error as a function of virtual crack positions in two steps of test part 1 (**Figure 6(a)**) and test part 2 (**Figure 6(b)**). The parabolic shape of the curves highlights the presence of a global minimum, which is the best approximation of the position of the crack tip.

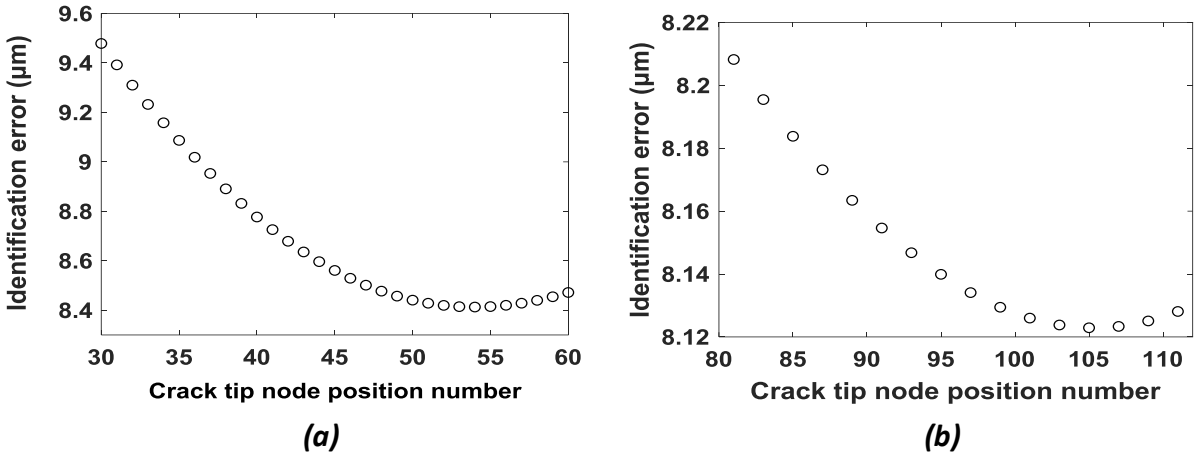

Figure 6: *Identification error as function of crack position for (a) step 563, and (b) step 626*

Procedures 1 and 2 were fully automated within a Matlab environment. In procedure 2, for each step (or image), an initial crack tip position was considered on the defined crack path. The crack tip was set to be at the position found in the previous image (starting from node 3 for the first image). Then, 5 simulations were conducted considering the selected position, the next 3 downstream and the previous upstream positions. The identification error was calculated for each simulation. If the error-tip position curve was not strictly decreasing, the crack tip position was the one with the smallest identification error. Otherwise (i.e. the error-tip curve is strictly decreasing), 5 new simulations were run in which the selected position is that with the lowest error of the previous calculations. For each simulation batch, the finite element calculations, the comparison between measured and calculated displacements and the error calculation lasted 5 minutes in all. Thus, for each image, procedure 2 took between 5 and 15 minutes (depending on the crack propagation increment) to locate the crack tip position. Compared to procedure 2, procedure 1 was faster especially at the beginning of the test when the only strain concentration zone is near the crack tip but when heterogeneities in the strain maps appears, the identification procedure becomes slower (for example, the application of procedure 1 on this test took 3 hours).

3.3 Results and discussion

3.3.1 Identification error analysis

Beyond the location of the crack tip, procedure 2 makes it possible to identify the domains of validity of the assumptions made in the FE model. Two regimes were observed when analyzing the identification error as a function of the loading steps (**Figure 7**). First, when there

was no crack on the surface of the material, the identification error did not exceed 2µm (**Figure 7(a)**, until step 562). It is explained by the fact that a purely elastic model was a good first order approximation of the sample behavior. Second, when reaching step 562, the crack initiated and propagated causing notch filament weld line failure (see Subsection 2.3). There was a sudden increase of the identification error (from 2 µm to 8.2 µm). This increase was due to the development of the fracture process zone that gave rise to nonlinearities confined in its vicinity. The perfectly elastic behavior assumed in the finite element model did not take into such phenomena so the computed strains in this area will be underestimated.

The propagation phase was analyzed in the second part of the test (**Figure 7(b)**). From step 566 on, a zoom was operated on the notch bottom vicinity. Thus image 566 is the new reference image for DIC, which resets the measured displacements. This reset explains the fact that the identification error again starts from very low values. The error increased in two stages. The first one, up to image 710, was a gradual growth because the largest part of the difference between the measured and computed displacements essentially came from the fracture process zone where increasingly pronounced plasticity took place. Beyond step 710, several areas of plastic deformation and damage appeared elsewhere than round the crack tip so that the error increased more rapidly. Heterogeneities in the strain maps were due to the structure of the material obtained by AM [32].

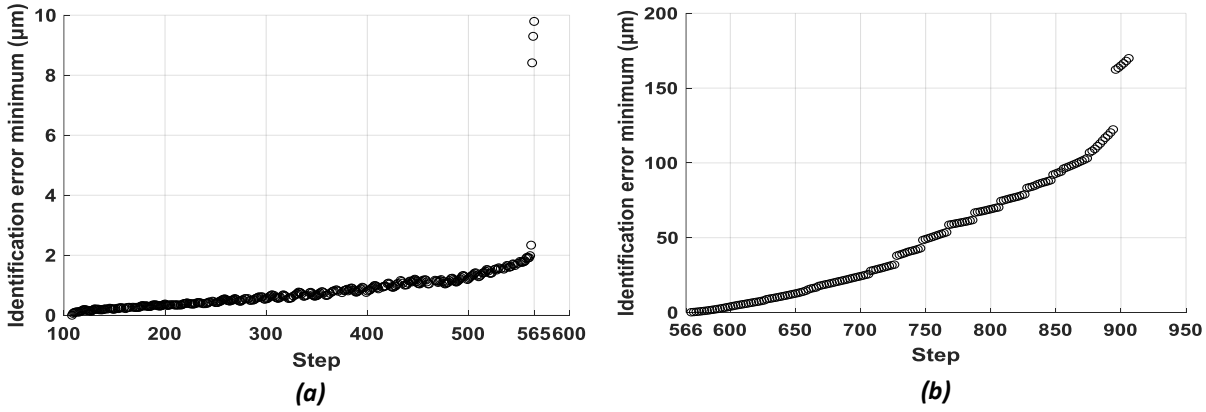

Figure 7: *Identification error for (a) test part 1, and (b) test part2*

3.3.2 Crack growth

Figure 8 shows the crack extension history obtained by applying both procedures. At the beginning of the test, no crack propagation was noticeable. Both methodologies had high uncertainties for the first steps due to the very small displacement ranges. Once reaching step

562, the crack initiated and propagated between the two filaments forming the edge of the notch. In the second part of the test (from step 565 on), the displacement fields were reset because of the magnification change. Despite small displacement levels, it was observed that the FE procedure identified smaller crack lengths than the strain field-based procedure. The presence of the crack did not necessarily cause discontinuities in the measured strain fields. For this reason, the first procedure did not detect crack growth on the first 70 images. From step 636 on, when the deformation becomes sufficiently large compared to a reference state (step 566) the propagation of the crack was detected. Beyond step 690, both procedures converged to similar values of Δa with a maximum offset of 6%. This analysis highlights the precision of the method based on FE analyses (procedure 2). Its ability to detect crack growth even in the case of small deformations is a strong advantage. This capability was useful in this study to be able to continue following the crack propagation even with a change in microscope magnification and with the re-initialized kinematic fields.

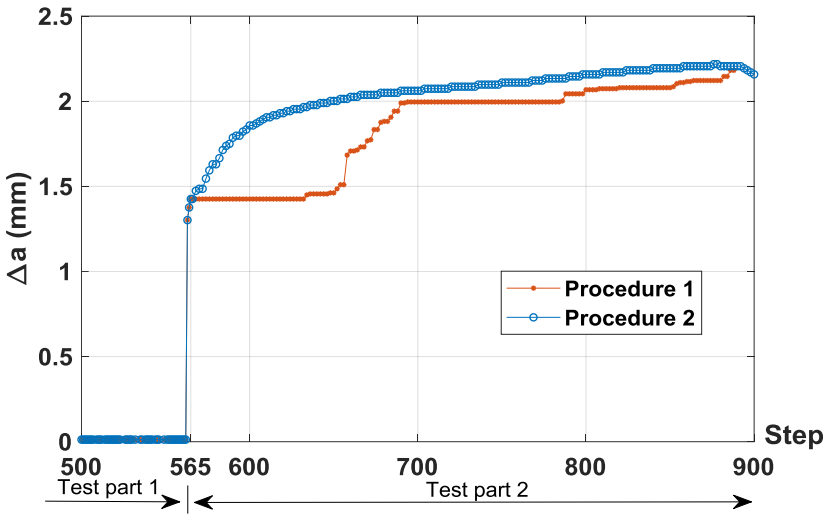

Figure 8: *Crack growth history determined by both procedures*

4 *J*-integral calculation

To evaluate the *J*-integral, experimentally measured displacement and strain fields via DIC were used. Then, the stresses are evaluated locally by assuming orthotropic elasticity to apply along the considered contour. Another route was provided by the FE code with its built-in (domain) procedure. In that case, measured Dirichlet boundary conditions are applied to the

elastic model. It is worth noting that the *J*-integral evaluations reported hereafter use contours or domains centered on the estimated crack tip positions by both procedures.

4.1 Methodology

To calculate the *J*-integral from measured displacement and strain fields, the stresses need to be evaluated. The parts fabricated by FDM were made layer by layer, which led to a mechanical behavior similar to that of laminated structures [53–55]. A plane stress assumption was made for each layer. In that case, the strain-stress relationship is written as

$$\begin{Bmatrix} \sigma_{xx} \\ \sigma_{yy} \\ \tau_{xy} \end{Bmatrix} = \begin{bmatrix} \overline{Q}_{11} & \overline{Q}_{12} & 0 \\ \overline{Q}_{12} & \overline{Q}_{22} & 0 \\ 0 & 0 & \overline{Q}_{66} \end{bmatrix} \begin{Bmatrix} \varepsilon_{xx} \\ \varepsilon_{yy} \\ \gamma_{xy} \end{Bmatrix} \tag{2}$$

where (x, y, z) is the global coordinate system, (1, 2, 3) the local coordinate system, $\overline{Q}_{ij}$ the components of the stiffness matrix calculated by using the transformation matrix, $[\mathbf{T}]$, between the two coordinate systems

$$[\mathbf{T}] = \begin{bmatrix} \cos^2\theta & \sin^2\theta & 2\cos\theta \times \sin\theta \\ \sin^2\theta & \cos^2\theta & -2\cos\theta \times \sin\theta \\ -\cos\theta \times \sin\theta & \cos\theta \times \sin\theta & \cos^2\theta - \sin^2\theta \end{bmatrix} \tag{3}$$

Then, $[\overline{\mathbf{Q}}]$ is written as

$$[\overline{\mathbf{Q}}] = [\mathbf{T}]^{-1}[\mathbf{Q}][\mathbf{T}]^{-T} \tag{4}$$

The *J*-integral is a measure of the energy release rate in a cracked medium and is expressed, in the form of a contour integral [20]

$$J = \oint_{\Gamma} \left(w\, dy - \mathbf{t} \frac{\partial \mathbf{u}}{\partial x} ds \right) \tag{5}$$

where Γ is a contour surrounding the notch tip, w the strain-energy density, $\mathbf{t}$ the traction defined with the outward normal along Γ, $\mathbf{u}$ the displacement vector, and s the curvilinear abscissa along Γ.

Several methods were proposed to calculate the *J*-integral experimentally [21,22,24]. They have not yet been applied to additively manufactured materials. Thanks to the similarity between these materials and composites, the formulation such as that proposed by Catalanotti et al. [21] may prove suitable for 3D printed materials. To calculate the *J*-integral in a composite material, the authors proposed a formulation derived from Rice's work [20]. It is calculated using

displacement, strain and stress data with a rectangular contour enclosing the crack tip. The *J*-integral was computed point-by-point along each edge of the contour [21]

$$J = \int_{\Gamma} \left(\frac{1}{2} \left\{ \bar{\boldsymbol{\sigma}} \right\} \left\{ \boldsymbol{\varepsilon} \right\}^{T} n_1 - \left\{ \frac{\partial \mathbf{u}}{\partial x_1} \right\}^{T} \left[\bar{\boldsymbol{\sigma}} \right] \left\{ \mathbf{n} \right\} \right) ds \tag{6}$$

where $\left\{ \bar{\boldsymbol{\sigma}} \right\}$ is the average stress vector, $\left\{ \boldsymbol{\varepsilon} \right\}$ the corresponding strains, $\left\{ \mathbf{n} \right\}$ the contour normal, n_1 the contour normal in the crack direction, and $\left\{ \partial \mathbf{u} / \partial x_1 \right\}$ the displacement gradient. The µ-SENT sample was made by a succession of +45° and -45° layers. The average stresses were computed from the transformed stiffness matrices of the +45° and -45° plies, $\left[\bar{\mathbf{Q}}^{+45} \right]$ and $\left[\bar{\mathbf{Q}}^{-45} \right]$ respectively, as $\left\{ \bar{\boldsymbol{\sigma}} \right\} = \frac{1}{2} \left(\left[\bar{\mathbf{Q}}^{+45} \right] + \left[\bar{\mathbf{Q}}^{-45} \right] \right) \left\{ \boldsymbol{\varepsilon} \right\}$. The derivative of the displacement fields was calculated as

$$\left\{ \frac{\partial \mathbf{u}}{\partial x_1} \right\} \approx \left\{ \frac{\Delta \mathbf{u}}{\Delta x_1} \right\} = \left\{ \frac{\mathbf{u}^{i+1} - \mathbf{u}^{i-1}}{2 \Delta x_1} \right\} \tag{7}$$

The *J*-integral was then assessed from the sum of all discrete contributions of each subset center.

In the present case, contour integrals were used to evaluate *J*. An alternative route is to resort to domain integrals [56–58]. This path was not followed in this first procedure because nonlinearities were suspected to occur in the vicinity of the crack tip. Conversely, procedure 2 utilized built-in methods of the selected FE code.

4.2 Method validation

Since the *J*-integral is path independent [20], different contours were considered. Further, the method was also applied to displacement and strain fields obtained by a finite element calculation. Then the *J*-integral was computed based on kinematic fields obtained by DIC measured on the surface of the specimen.

4.2.1 Application with FE kinematic fields

DIC measured displacements were taken as boundary conditions and the FE code computed displacements and strains over the considered surface (**Figure 5**). Based on these computed fields, the *J*-integral was calculated using both methods described above. Twenty-five contours were chosen in the crack tip vicinity area. The first contour (contour 45) was positioned at a distance of 270 µm from the crack tip and the last one (contour 70) at 420 µm. This area was

chosen far enough from the crack tip to avoid possible nonlinearities. The strategy for constructing and naming these contours is described in **Figure 9(a)**. Contour *N* is a square centered about the crack tip and passing through the N^{th} crack path node to the right. The *J*-integral levels calculated on these contours are compared in **Figure 9(b**) to those determined directly by the FE code [31]. Both methods give constant values for all selected contours. Last, there was a systematic offset of 4% between the two methods. This was level was considered sufficiently small to validate the present implementation.

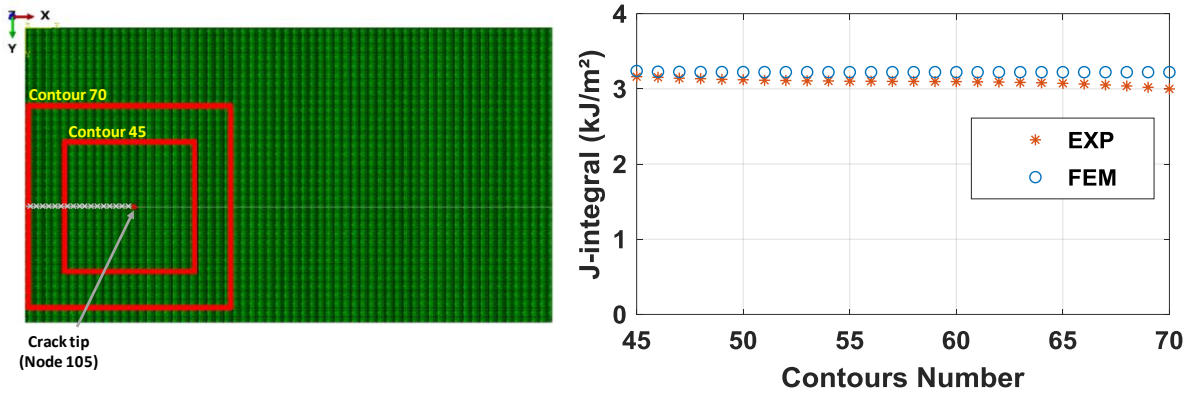

(a) *(b)*

Figure 9: *(a) Contours selected to calculate the J-integral. (b) J-integral as a function of contour number (step 666) for both procedures.*

4.2.2 Application to experimental fields

Kinematic fields measured by DIC were used to calculate the *J*-integral on several contours with procedure 1. **Figure 10** shows the effect of the contour position on the *J*-integral computed at step 666. The levels of the *J*-integral of the closest contours to the singularity were not taken into consideration [24]. Large deformations in that area may bias the results [59,60]. For contours located farther away from the crack tip, the results were close with a gap not exceeding 1.7%. The contour independence confirms that the computation of the *J*-integral in an AM polymeric material can be made by following the method based on DIC measured fields. This method

was presented in the literature as being independent of the crack tip location, by considering a contour large enough to contain the crack tip throughout the test [22,23].

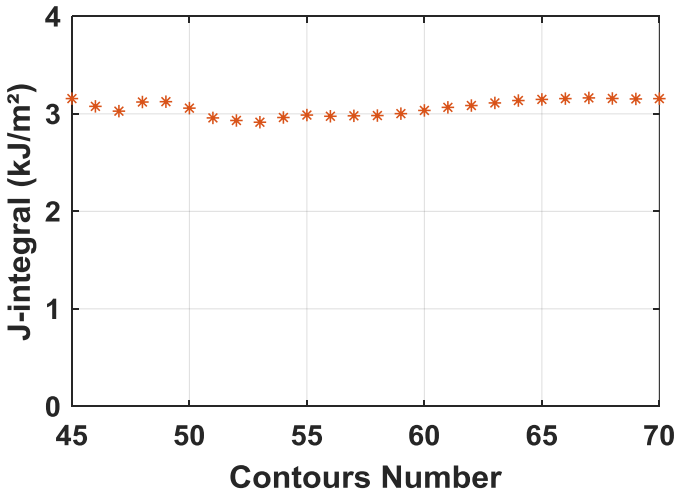

Figure 10: *J-integral as function of contours number (step 666)*

Such approach makes it possible to obtain the change of *J* without necessarily locating the point of the crack tip, a task that may be complicated to carry out. Thanks to the two procedures of crack tip location presented in Section 2, the effect of crack tip location on the level of *J* can be analyzed. This task will be the subject of the next section.

4.3 Results and discussions

4.3.1 Crack tip location effect

The *J*-integral was computed by contour integration using experimentally measured strains and displacements. Both crack extension laws (**Figure 8**) were considered. For each load step, the contour was placed in such a way that it contained the crack tip while ensuring that most of the surface it covered was in front of the crack tip.

Figure 11 shows the *J*-integral history in both parts of the test. At the beginning of the test (**Figure 11(a)**), the *J*-integral was null because no crack was detected on the surface of the material until step 540. From this step on, strain concentrations occurred at the location where the crack initiated. This phase, which preceded the actual initiation (between steps 540 and 562), gave rise to nonzero values of *J* that remained very low (i.e., less than 0.2 kJ/m²) until the initiation of the crack at step 563, which caused a significant increase in *J*. It is recalled

here that in this test the measured fields were reinitialized at step 565 to zoom in around the crack vicinity. At this step, the *J*-integral was also reset, and referred to ΔJ.

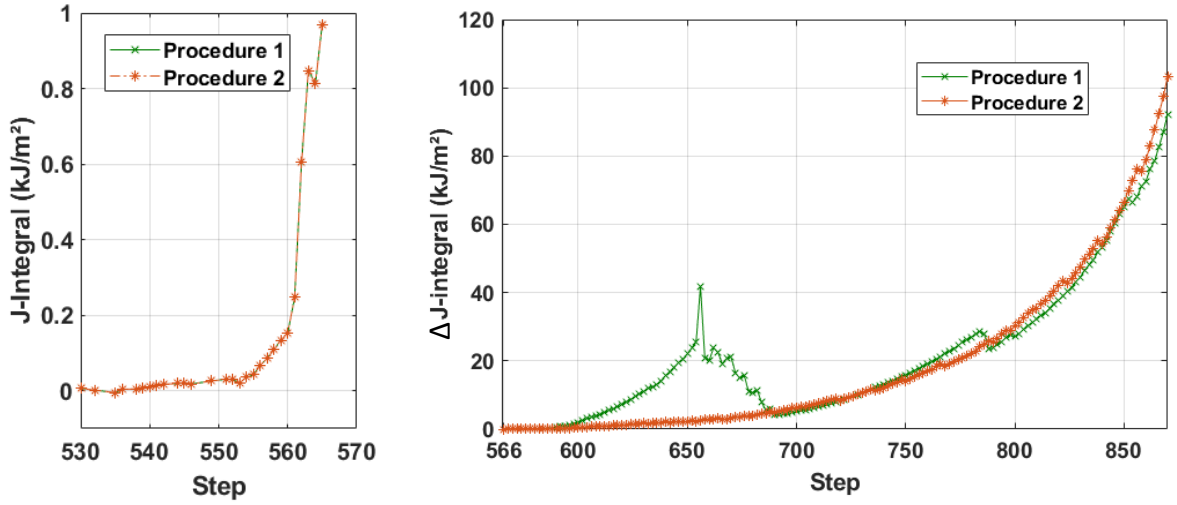

Test part 1 *Test part 2*

Figure 11: *J-integral calculated by experimental method on both test parts with crack tip location given by the two proposed procedures*

During the second part of the test, the value of ΔJ increased continuously when using the crack tip location given by procedure 2 [29] (**Figure 11(b)**). The curve took the expected shape of the variation of ΔJ as a function of the load applied to the tested sample [24,61]. However, this was not the case using the position of the crack tip given by procedure 1. Results in **Figure 11(b)** (green curve) show a discrepancy appearing between steps 600 and 700 where the value of *J* increased abnormally before suddenly falling off. This trend was due to bad positioning of the integration contour. During this period of time, the contour was not correctly placed around the crack tip but rather downstream by a significant amount (see **Figure 8** between steps 600 and 700) and this is confirmed by the variation curve of ΔJ. Last, given the level of *J* at the end of the first part (i.e. of the order of 1 kJ/m^2) and that observed in the second part (tens of kJ/m^2), the increment ΔJ is very close to the total fracture energy.

It emerges from this analysis that the experimental method of calculating *J* directly from kinematic fields measured by DIC can be applied to AM polymeric materials. Yet, its accuracy depends on integration contour location. It therefore required to be assisted by an accurate method of locating the crack tip around which this contour will be placed. In the next section,

a comparison will be carried out between the results given by this method and those obtained by FE simulations for the same crack tip location.

4.3.2 Experimental vs. FE evaluations of J

The finite element model established to follow crack growth (procedure 2) calculated at each step the *J*-integral with the built-in procedure of the FE code [34]. The *J*-integral variation is compared in **Figures 12** and **14** to those obtained by the experimental method based on DIC measurements. The results of the two parts of the test are analyzed separately. The crack tip position given by procedure 2 was considered as it was deemed more reliable than the strain-based procedure.

- **Test part 1**

A similarity is noted when comparing the results given by the experimental method and the FE computations. Both methods detect a very low level of *J* in this part of the test but its variation was different. For the experimental method (procedure 1), *J* remained equal to zero, and non-zero values were measured only a few instants before initiation, which was not the case for the FE-based procedure (2). The calculation gave nonzero values of *J* early in the test even though the crack was physically nonexistent. Despite the very low values, it was interesting to investigate the possible causes of such differences. From the results of **Figure 8**, the initiation instant was defined as the first nonzero crack increment. The initiation time is depicted with the dashed box in **Figure 12** and leads to a value of *J* less than 1 kJ/m².

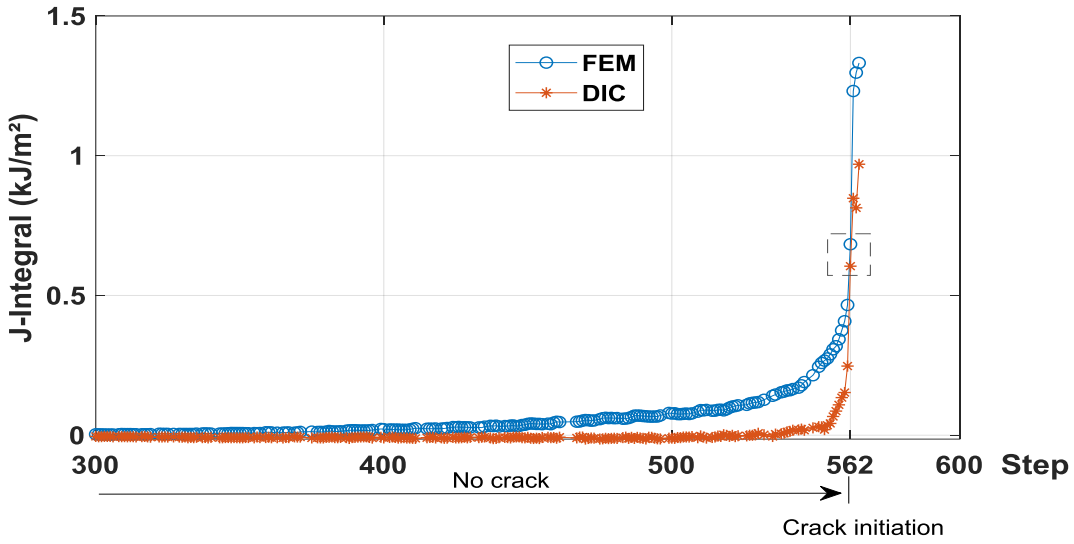

Figure 12: *J-integral variation for the two procedures (experimental and FE). The dashed box depicts the estimated initiation instant.*

In the finite element model established to find the crack tip position (procedure 2), the crack path was preset and at least one node was split. Each node on this path could be chosen as crack tip but only one node gave the minimum value of the displacement residual and it was the best approximation for crack tip location. When the modeled surface (i.e., the ROI chosen in DIC, see **Figure 5**) was free from any crack, the node for which the error will be minimal was that located on the left edge of the surface. The crack tip was thus located numerically on the edge of the ROI while physically it may lie outside the ROI. This shift was at the origin of the overestimation of the *J*-integral obtained numerically compared to the experimental method values. To confirm this hypothesis, a second calculation was run using an elastic calculation driven by the measured boundary conditions with no crack. The identification error between the measured and computed displacements of the second FE simulation, $\delta(\text{no crack})$, was calculated for each load step. Then, it was compared to the error of the initial model (with crack) by plotting the variation of the error difference

$$\Delta = \sqrt{\frac{1}{n_m}\sum_{m=1}^{n_m}\left\|\mathbf{u}_{meas}(\mathbf{x}_m)-\mathbf{u}_{comp}(\mathbf{x}_m,\mathbf{x}_c=0)\right\|^2} - \sqrt{\frac{1}{n_m}\sum_{m=1}^{n_m}\left\|\mathbf{u}_{meas}(\mathbf{x}_m)-\mathbf{u}_{comp}(\mathbf{x}_m,\text{no crack})\right\|^2} \quad (8)$$

When $\Delta > 0$, the solution with no crack is likelier than that with a small crack. Conversely, when $\Delta < 0$, the solution with a crack is more trustworthy. For each step, the values of Δ are reported in **Figure 13(a).** At the beginning of the test, the error difference Δ was very small. Then, the difference between the two models was more important, in favor of the model with

no crack. From image 562 on, the initiation of the crack changed the trend, and therefore the model with no crack was less consistent with the experiment. This observation confirms that the choice of a point of the crack on the edge of the ROI caused an overestimation of *J* compared to that obtained by the experimental method. The corrected *J*-curve is equal to zero up to image 562 (FEM' in **Figure 13(b)**, and after that it coincides with the previous results. This new estimation of the initiation time is consistent with what was obtained with the crack extension (**Figure 12**). It is worth noting that this additional analysis was conducted thanks to the results provided by the first procedure. Had it not been utilized, such additional study would probably not have been undertaken.

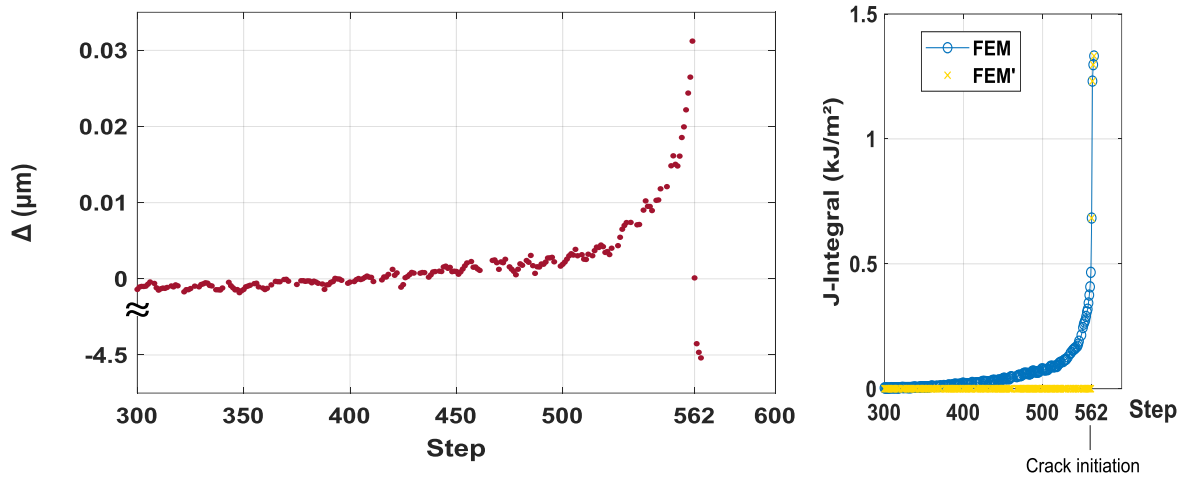

(a) *(b)*

Figure 13: *(a) Difference in identification error for the two models for the first part of the test. (b) J-integral obtained with procedure 2 when assuming the presence of the crack right from the beginning of the test (procedure 2) or only when Δ < 0 (procedure 2')*

Figure 14 shows a comparison between the measured and computed longitudinal displacement fields for key load steps of the first part of the test by reporting the residual map. These maps are compared with the variation of *J* as well as the identification error. The error maps show that the displacements were consistent with the experiment since the residuals were small (i.e. δ less than 2 µm). This means that the behavior of the material introduced in the model and the boundary conditions achieved a good level of accuracy. From step 560 on, a process zone appeared and became more evident at step 562 in which the behavior of the material was no longer elastic close to the crack tip. In 3 s, the welding joint between the

filaments of the contour forming the notch was broken and the crack was open. The presence of the notch and the gradual loading created a process zone located at the crack tip (**Figure 14**, step 565). Plasticity was confined in the immediate vicinity of the crack tip, its impact on the *J*-integral remained minimal because the contour on which *J* was calculated was large.

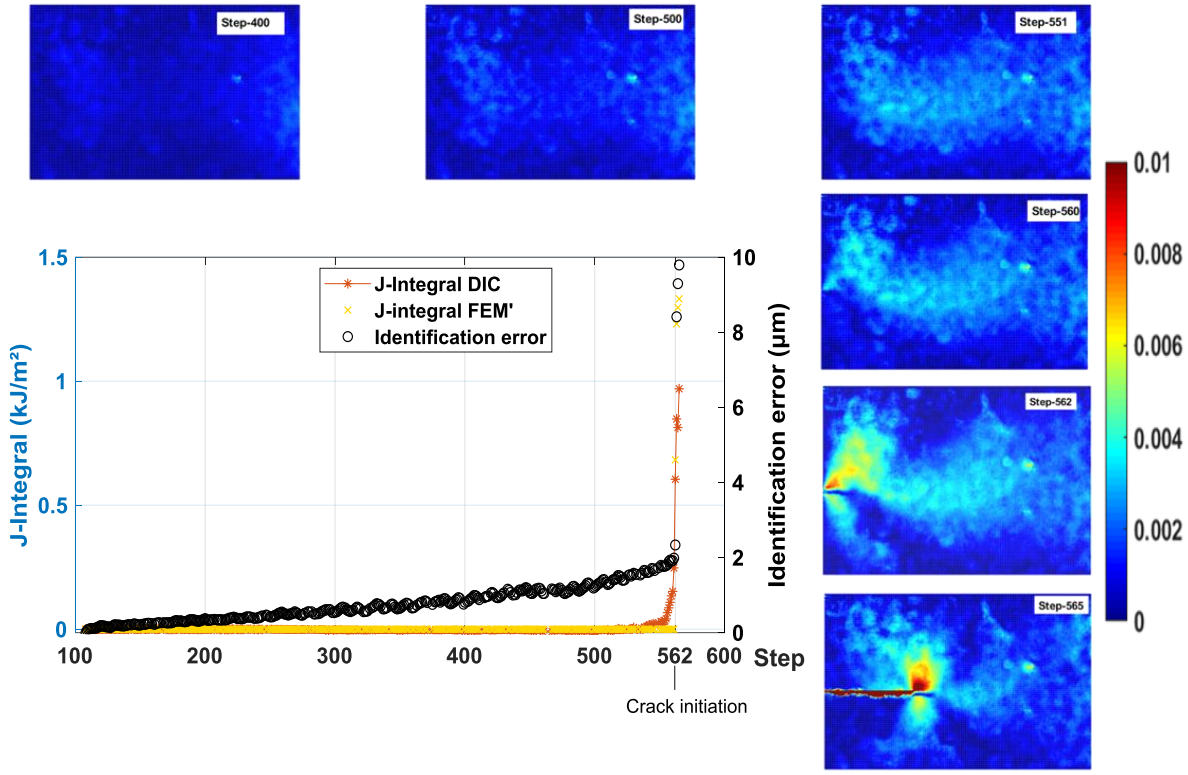

Figure 14: *Residual displacement fields (mm) for different load steps for the first part of the test*

4.3.2.1 Test part 2

In the second part of the test, from the kinematic fields measured at the surface of the material the *J*-integral was calculated using both methods (**Figure 15**). Until step 772, both methods yielded almost the same levels of *J* (Root Mean Squared Error = 0.46 kJ/m²). From step 772 on, the results diverge, namely, the experimental procedure gave higher values of *J* than those computed by the FE-based procedure. In section 2, when analyzing identification error variations in the second part of the test, a first assumption was made regarding the origin of the offset between experimental and computed fields (i.e., nonlinearities in the process zone). For higher levels, plastic deformations and damage appeared elsewhere than around the crack tip (**Figure 2**) so that the error between measured and computed displacements and strains increased, which led to the *J*-integral offset.

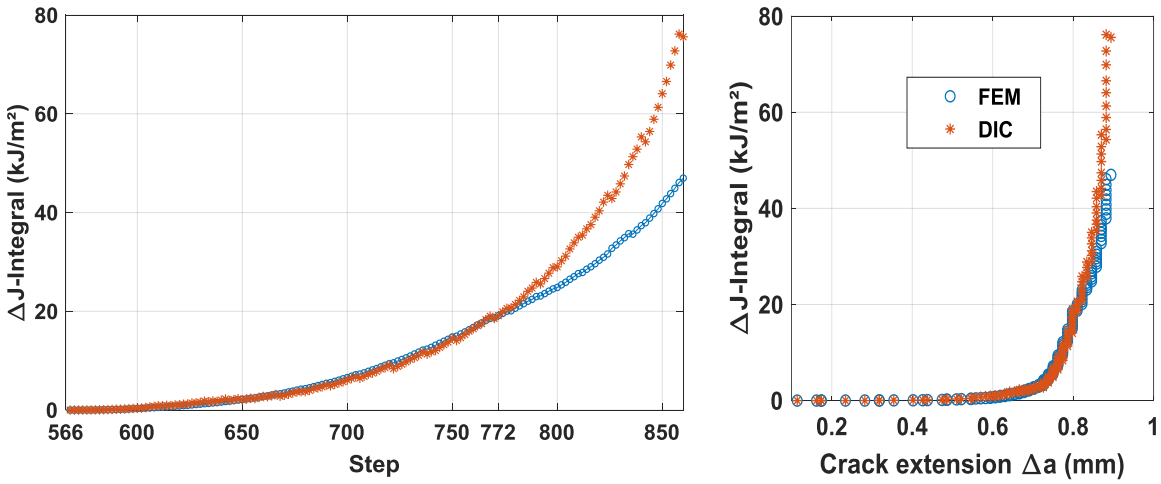

(a) *(b)*

Figure 15: *(a) J-integral changes using both procedures with the same crack tip location. (b) Corresponding ΔJ-R curves.*

Residual longitudinal displacements maps reported in **Figure 16** evidence these effects. For relatively low loads (e.g. step 650), the FE model described rather well the material behavior and the identification error in displacement did not exceed 13 µm. The evaluation of the *J*-integral by both methods yielded almost the same level. From step 772 on, the plastic deformation extended to locations other than the crack tip vicinity, which made the FE model not very precise because it did not consider the plastic behavior. This is also true for the experimental procedure in which the stress levels were overestimated since they were computed by using the total strains evaluated via DIC. In the FE model, the computed value of *J* related only to the main crack whereas in the experimental method it included nonlinear deformations that appeared elsewhere in the specimen.

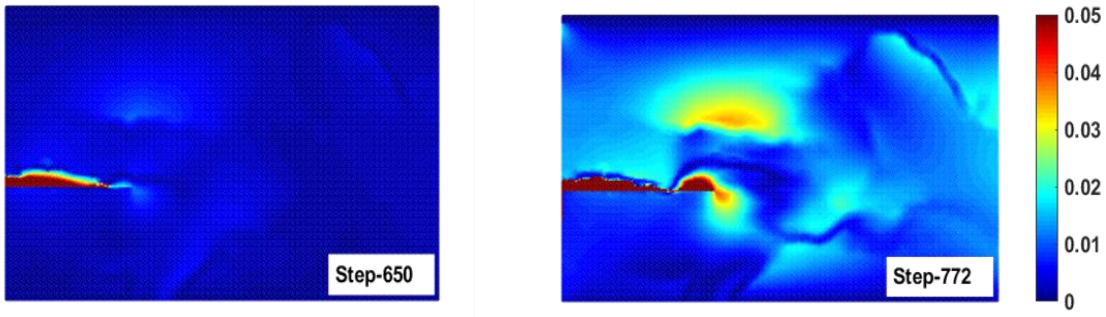

Figure 16: *Residual longitudinal displacement fields (mm) for two steps of the second part of the test.*

5 Conclusion

In order to standardize investigations on the fracture behavior of additively manufactured polymeric materials, simple, automatic, and accurate methods for evaluating the *J*-integral and crack growth were examined. The first one evaluated the contour integral with measured displacement and strain fields, then computed the stresses. The second one considered measured displacements used as boundary conditions of finite element simulations. The crack tip position was found by minimizing the error between computed and measured displacement fields of the inner nodes. The *J*-integral was obtained with the built-in interaction integral.

Both methods were applied to a micro Single Edge Notched Tensile (μ-SENT) sample manufactured by fused filament fabrication (FFF) of acrylonitrile butadiene styrene (ABS). It was shown that the *J*-integral could be obtained accurately by both methods during most of the propagation regime. The FE-based method showed very high robustness to accurately locate the crack tip. The crack length was quantified in an automatic way that did not require any visual inspection, and the *J*-integral calculation was based on local measurements and thus made it possible to obtain *J*-*R* curves independently of the specimen geometry. It is worth noting that these methods do not need any a priori calibration for the calculation of *J*.

The analysis of the initiation regime showed that the experimental procedure could better capture the early initiation process. It allowed the numerical procedure to be supplemented by an additional analysis with no crack. It was then shown that for a long time the model with no crack was as trustworthy as that with a crack. From such analysis, the initiation time was shown to be fully consistent with its estimate based on the crack advance.

The investigated procedures were shown to be well adapted to polymeric 3D printed materials and gave access to micrometer scales that have an important effect on the mechanical properties of such materials. The applicability of these methods is not limited to the identification of fracture properties of AM polymer parts but can also be extended to mechanical properties such as their constitutive law. The FE-based method applied in this study makes it possible to locally check the validity of the elastic properties or even enrich the model to describe the nonlinear behavior in the process zone. This was made possible by comparing computed displacements to those measured via DIC. It can be done in two ways. First, by following the changes of the identification error during the test. As illustrated herein, various model hypotheses could be probed. Second, by computing difference maps between numerical and experimental displacement fields. These maps allow links between the underlying microstructure and the mechanical properties to be established.

6 Acknowledgments

This work was supported by Region Grand Est (France) via the funding NANO – FAB (18 - GES – 027) Soutien aux jeunes chercheurs.

7 Statement of contributions

M.A. BOUAZIZ, J. MARAE DJOUDA and F. HILD conceived the presented idea. J. GARDAN and M. ZOUAOUI manufactured the samples.J. MARAE DJOUDA carried out the experiment. M.A. BOUAZIZ processed the experimental data, performed the analysis, drafted the manuscript and designed the figures. F. HILD and J. MARAE DJOUDA supervised and guided the investigations and contributed to the development of the method. They also aided M.A. BOUAZIZ in interpreting the results and worked on the manuscript. All authors commented on the manuscript.

8 References

1 Attaran M. The rise of 3-D printing: The advantages of additive manufacturing over traditional manufacturing. *Bus Horiz*. 2017;60: 677–688.

2 Tofail SAM, Koumoulos EP, Bandyopadhyay A, Bose S, O'Donoghue L, Charitidis C. Additive manufacturing: scientific and technological challenges, market uptake and opportunities. *Mater Today*. 2018;21: 22–37.

3 Ivanova O, Williams C, Campbell T. Additive manufacturing (AM) and nanotechnology: Promises and challenges. *Rapid Prototyp J*. 2013;19: 353–364.

4 Gardan J. Additive manufacturing technologies: State of the art and trends. *Int J Prod Res*. 2015;7543: 149–168.

5 Turner BN, Strong R, Gold SA. A review of melt extrusion additive manufacturing processes: I. Process design and modeling. *Rapid Prototyp J*. 2014;20: 192–204.

6 Durgun I, Ertan R. Experimental investigation of FDM process for improvement of mechanical properties and production cost. *Rapid Prototyp J*. 2014;20: 228–235.

7 Balderrama-Armendariz CO, MacDonald E, Espalin D, Cortes-Saenz D, Wicker R, Maldonado-Macias A. Torsion analysis of the anisotropic behavior of FDM technology. *Int J Adv Manuf Technol*. 2018;96: 307–317.

8 Sood AK, Ohdar RK, Mahapatra SS. Experimental investigation and empirical modelling of FDM process for compressive strength improvement. *J Adv Res*. 2012;3: 81–90.

9 Vairis A, Petousis M, Vidakis N, Savvakis K. On the Strain Rate Sensitivity of Abs and Abs Plus Fused Deposition Modeling Parts. *J Mater Eng Perform*. 2016;25: 3558–3565.

10 Sun Q, Rizvi GM, Bellehumeur CT, Gu P. Effect of processing conditions on the bonding quality of FDM polymer filaments. *Rapid Prototyp J*. 2008;14: 72–80.

11 Ahn SH, Montero M, Odell D, Roundy S, Wright PK. *Anisotropic Material Properties of Fused Deposition Modeling ABS*. Vol 8.2002.

12 Cantrell JT, Rohde S, Damiani D, et al. Experimental characterization of the mechanical properties of 3D-printed ABS and polycarbonate parts. *Rapid Prototyp J*. 2017;23: 811–824.

13 Rezayat H, Zhao W, Siriruk A, Penumadu D, Babu SS. Structure – mechanical property relationship in fused deposition modelling. *Mater Sci Technol*. 2015;31(8): 895–903.

14 Chacón JM, Caminero MA, García-Plaza E, Núñez PJ. Additive manufacturing of PLA structures using fused deposition modelling: Effect of process parameters on mechanical properties and their optimal selection. *Mater Des*. 2017;124: 143–157.

15 Cuan-Urquizo E, Barocio E, Tejada-Ortigoza V, Pipes RB, Rodriguez CA, Roman-Flores A. Characterization of the mechanical properties of FFF structures and materials: A review on the experimental, computational and theoretical approaches. *Materials (Basel)*. 2019;16.

16 Zaldivar RJ, Witkin DB, McLouth T, Patel DN, Schmitt K, Nokes JP. Influence of processing and orientation print effects on the mechanical and thermal behavior of 3D-Printed ULTEM ® 9085 Material. *Addit Manuf*. 2017;13: 71–80.

17 Hart KR, Wetzel ED. Fracture behavior of additively manufactured acrylonitrile

butadiene styrene (ABS) materials. *Eng Fract Mech*. 2017;177: 1–13.

18 McLouth TD, Severino J V., Adams PM, Patel DN, Zaldivar RJ. The impact of print orientation and raster pattern on fracture toughness in additively manufactured ABS. *Addit Manuf*. 2017;18: 103–109.

19 Li J, Yang S, Li D, Chalivendra V. Numerical and experimental studies of additively manufactured polymers for enhanced fracture properties. *Eng Fract Mech*. 2018;204: 557–569.

20 Rice JR. A Path Independent Integral and the Approximate Analysis of Strain Concentration by Notches and Cracks. *J Appl Mech*. 1968;35: 379.

21 Catalanotti G, Camanho PP, Xavier J, Dávila CG, Marques AT. Measurement of resistance curves in the longitudinal failure of composites using digital image correlation. *Compos Sci Technol*. 2010;70: 1986–1993.

22 Becker TH, Mostafavi M, Tait RB, Marrow TJ. An approach to calculate the J-integral by digital image correlation displacement field measurement. *Fatigue Fract Eng Mater Struct*. 2012;35: 971–984.

23 Becker TH, Marrow TJ, Tait RB. Damage, crack growth and fracture characteristics of nuclear grade graphite using the Double Torsion technique. *J Nucl Mater*. 2011;414: 32–43.

24 Yoneyama S, Arikawa S, Kusayanagi S, Hazumi K. Evaluating J-integral from displacement fields measured by digital image correlation. *Strain*. 2014;50: 147–160.

25 J. W. Hutchinson. Singular Behaviour at The End of a Tensile Crack in a Hardening Materail. *J Mech Phys Solids*. 1978;16: 13–31.

26 Lanzillotti P, Gardan J, Makke A, Recho N. Enhancement of fracture toughness under mixed mode loading of ABS specimens produced by 3D printing. *Rapid Prototyp J*. 2019;25: 679–689.

27 Nishioka T, Ikegita H, Tamai K, Kobayashi N. An Incremental Variational Principle Minimizing Experimental Measurement Errors and Its Application to an Intelligent Hybrid Experimental-Numerical Method. Case of Nonlinear Elastic-Plastic Deformation Field. *JSME Int J Ser A*. 2001;44: 71–81.

28 Hareesh T V., Chiang FP. Integrated experimental-finite element approach for studying elasto-plastic crack-tip fields. *Eng Fract Mech*. 1988;31: 451–461.

29 Mathieu F, Aimedieu P, Guimard JM, Hild F. Identification of interlaminar fracture properties of a composite laminate using local full-field kinematic measurements and finite element simulations. *Compos Part A Appl Sci Manuf*. 2013;49: 203–213.

30 Barhli SM, Mostafavi M, Cinar AF, Hollis D, Marrow TJ. J-Integral Calculation by Finite Element Processing of Measured Full-Field Surface Displacements. *Exp Mech*. 2017;57: 997–1009.

31 Djouda JM, Gallittelli D, Zouaoui M, et al. Local scale fracture characterization of an advanced structured material manufactured by fused deposition modeling in 3D printing. *Frat ed Integrita Strutt*. 2020;14: 534–540.

32 Djouda JM, Ali Bouaziz M, Zouaoui M, et al. Experimental approach for microscale mechanical characterization of polymeric structured materials obtained by additive manufacturing. *Polym Test*. May 2020: 106634.

33 SIMULIA. ABAQUS/Standard Version 6.18 Analysis User's Manual. 2018.

34 Simulia. Contour integral evaluation (Section 11.4.2). Abaqus Analysis User's Manual.

35 Brocks W, Scheider I. Numerical Aspects of the Path-Dependenceof the J-Integral in Incremental Plasticity How to Calculate Reliable J-Values in FE Analyses. *Int J Fatigue*. 2001: 1–33.

36 ASTM-E1820–11. Standard test method for measurement of fracture toughness. In: *ASTM, Annual Book of Standards 3*. ; 2011.

37 ASTM-6068. Standard Test Method for Determining J-R Curves of Plastic Materials. *ASTM Stand Test Method*. 2013;i: 1–8.

38 Bruck HA, McNeill SR, Sutton MA, Peters WH. Digital image correlation using Newton-Raphson method of partial differential correction. *Exp Mech*. 1989;29: 261–267.

39 Forquin P, Rota L, Charles Y, Hild F. A method to determine the macroscopic toughness scatter of brittle materials. *Int J Fract*. 2004;125: 171–187.

40 M. Sutton, W. Zhao, S. McNeill, J. Helm, R. Piascik and WR. Local crack closure measurements: Development of a measurement system using computer vision and a far-field microscope. *Adv fatigue crack Clos Meas Anal Second Vol ASTM Int*. 1999.

41 Blaber J, Adair B, Antoniou A. Ncorr: Open-Source 2D Digital Image Correlation Matlab Software. *Exp Mech*. 2015;55: 1105–1122.

42 Pan B. Full-field strain measurement using a two-dimensional Savitzky-Golay digital differentiator in digital image correlation. *Opt Eng*. 2007;46: 033601.

43 Roux S, Réthoré J, Hild F. Digital image correlation and fracture: An advanced technique for estimating stress intensity factors of 2D and 3D cracks. *J Phys D Appl Phys*. 2009;42.

44 Beevers C. Advances in crack length measurement. *Eng Mater Advis Serv*. 1982.

45 Hild F, Roux S. Digital image correlation: From displacement measurement to identification of elastic properties - A review. *Strain*. 2006;42: 69–80.

46 Hamam R, Hild F, Roux S. Stress intensity factor gauging by digital image correlation: Application in cyclic fatigue. *Strain*. 2007;43: 181–192.

47 Réthoré J, Roux S, Hild F. An extended and integrated digital image correlation technique applied to the analysis of fractured samples: The equilibrium gap method as a mechanical filter. *Eur J Comput Mech*. 2009;18: 285–306.

48 Mathieu F, Hild F, Roux S. Image-based identification procedure of a crack propagation law. *Eng Fract Mech*. 2013;103: 48–59.

49 Nguyen TL, Hall SA, Vacher P, Viggiani G. Fracture mechanisms in soft rock: Identification and quantification of evolving displacement discontinuities by extended digital image correlation. *Tectonophysics*. 2011;503: 117–128.

50 Grédiac M, Hild F. Full-field measurements and identification in solid mechanics. 2012.

51 Vargas R, Neggers J, Canto RB, Rodrigues JA, Hild F. Comparison of two full-field identification methods for the wedge splitting test on a refractory. *J Eur Ceram Soc*. 2018;38: 5569–5579.

52 Zouaoui M, Labergere C, Gardan J, et al. Numerical prediction of 3d printed specimens

based on a strengthening method of fracture toughness. *Procedia CIRP*. 2019;81: 40–44.

53 Somireddy M, Czekanski A. Mechanical Characterization of Additively Manufactured Parts by FE Modeling of Mesostructure. *J Manuf Mater Process*. 2017;1: 18.

54 Casavola C, Cazzato A, Moramarco V, Pappalettere C. Orthotropic mechanical properties of fused deposition modelling parts described by classical laminate theory. *Mater Des*. 2016;90: 453–458.

55 Zhao Y, Chen Y, Zhou Y. Novel mechanical models of tensile strength and elastic property of FDM AM PLA materials: Experimental and theoretical analyses. *Mater Des*. 2019;181: 108089.

56 Réthoré J, Gravouil A, Morestin F, Combescure A. Estimation of mixed-mode stress intensity factors using digital image correlation and an interaction integral. *Int J Fract*. 2005;132: 65–79.

57 Réthoré J, Roux S, Hild F. Noise-robust stress intensity factor determination from kinematic field measurements. *Eng Fract Mech*. 2008;75: 3763–3781.

58 Réthoré J, Roux S, Hild F. Optimal and noise-robust extraction of Fracture Mechanics parameters from kinematic measurements. *Eng Fract Mech*. 2011;78: 1827–1845.

59 Courtin S, Gardin C, Bézine G, Ben Hadj Hamouda H. Advantages of the J-integral approach for calculating stress intensity factors when using the commercial finite element software ABAQUS. *Eng Fract Mech*. 2005;72: 2174–2185.

60 Bouaziz MA, Guidara MA, Schmitt C, Hadj-Taïeb E, Azari Z, Dmytrakh I. Structural integrity analysis of HDPE pipes for water supplying network. *Fatigue Fract Eng Mater Struct*. 2019;42: 792–804.

61 Vavrik D, Jandejsek I. Experimental evaluation of contour J integral and energy dissipated in the fracture process zone. *Eng Fract Mech*. 2014;129: 14–25.